Thermal Stability of Spherical Nanoporous Aggregates and Formation of Hollow Structures by Sintering—A Phase-Field Study

Rajdip Mukherjee,[†] Tamoghna Chakrabarti,[†] Erumpukuthickal Ashok Anumol,[‡] Thennathur Appandairajan Abinandanan,[†,*] and Narayanan Ravishankar[‡,*]

[†]Department of Materials Engineering and [‡]Materials Research Centre, Indian Institute of Science, Bangalore 560012, India

ABSTRACT Nanoporous structures are widely used for many applications and hence it is important to investigate their thermal stability. We study the stability of spherical nanoporous aggregates using phase-field simulations that explore systematically the effect of grain boundary diffusion, surface diffusion, and grain boundary mobility on the pathways for microstructural evolution. Our simulations for different combinations of surface and GB diffusivity and GB mobility show four distinct microstructural pathways en route to 100% density: multiple closed pores, hollow shells, hollow shells with a core, and multiple interconnected pores. The microstructures from our simulations are consistent with experimental observations in several different systems. Our results have important implications for rational synthesis of hollow nanostructures or aggregates with open pores, and for controlling the stability of nanoporous aggregates that are widely used for many applications.

KEYWORDS: nanoporous · hollow structures · phase field simulation · surface diffusion · grain boundary diffusion · grain boundary mobility

Porous structures with accessible interior volumes are widely used in many applications ranging from catalysis to drug delivery. While structures with hollow interiors and surface-connected pores have unique properties which make them suitable candidates for various applications in the field of size-selective reactions, catalysis, drug delivery, and bioencapsulation,[1−7] recent reports have shown that hollow structures with closed outer shells could have strengths approaching the theoretical ideal shear strength.[8] The primary problem associated with such mesoporous structures with high surface areas is their instability against coarsening that leads to a rapid loss in the catalytic activity by sintering or to a degradation of other useful attributes. While the coarsening behavior of discrete particles supported on a substrate is well understood,[9−11] the thermal stability of mesoporous structures has not been investigated.

Recent experimental work demonstrated that partial sintering of mesoporous aggregates of nanocrystallites of several different metals/oxides leads to the formation of hollow structures indicating that the coarsening of such aggregates leads to a rich variety of intermediate structures before the formation of a fully dense structure.[12] Here, we study this process and demonstrate the variety of structures that can be formed by using simulations based on a phase-field model of particle aggregates containing voids. The results not only have important implications for the stability of mesoporous aggregates for catalytic applications but also provide a rational framework for the synthesis of hollow structures by controlling the sintering process.

Sintering is driven by the reduction in total surface energy of the system and occurs by a net inward transport of atoms or a net outward transfer of vacancies resulting in the formation of a dense compact. However, recent experimental observations[12] on sintering of nanoporous aggregates of Pt, TiO_2, CeO_2, and SnO_2 as illustrated in Figure 1 show that hollow structures are often produced as an intermediate state before complete densification takes place. The starting state in all these cases is a nearly spherical aggregate (~100 to 200 nm diameter) that comprises nanoparticles of the order of 2−3 nm as illustrated in the case of CeO_2 in Figure 1a. An estimate of the packing fraction of the particles in the aggregate based on BET pore size and specific surface area shows that the packing fraction is typically larger than 60% in all the systems investigated. Heating the aggregate to higher temperatures leads to the formation of hollow structures with single or multiple pores which exhibit a wide range of grain sizes. While the grain size does not show

* Address correspondence to nravi@mrc.iisc.ernet.in, abinand@materials.iisc.ernet.in.

Received for review November 9, 2010 and accepted March 10, 2011.

Published online March 10, 2011
10.1021/nn103036q

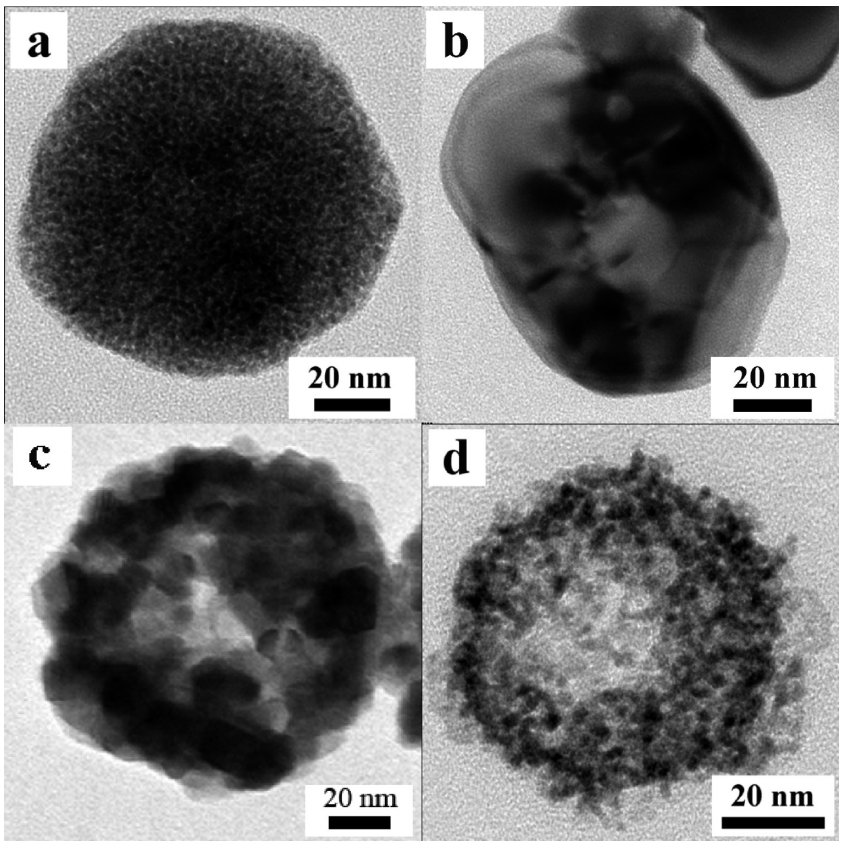

Figure 1. TEM bright field images of (a) as-synthesized porous aggregate of CeO_2, (b) hollow CeO_2 obtained by annealing the porous aggregate at 900 °C, (c) sintered SnO_2 aggregate, (d) sintered Pt aggregate (sintered at 500 °C).

appreciable change from the starting particle size in the case of Pt (Figure 1d), single crystalline hollow structures have been observed in the case of CeO_2. An intermediate structure with several tens of grains has been observed in the case of SnO_2 (Figure 1c). To understand the influence of various kinetic parameters on the evolution of microstructure and to delineate conditions under which the experimentally realized structures could be formed during the sintering of porous aggregate of nanocrystallites, a phase-field study is carried out on such a system.

The length scale of the above problem is in mesoscale regime and the mechanism involves atomic diffusion; hence phase-field modeling technique is the most suitable choice for modeling this phenomenon. Moreover this modeling technique correctly captures the Gibbs–Thomson effect which plays a significant role in microstructure evolution of nanoporous aggregates. From the kinetic point of view, the model is also capable of incorporating diffusivities (which correspond to atomic mobilities) along different paths of the microstructure (bulk, grain boundary and surface) and the grain boundary mobility, which play a key role in the temporal evolution of the system.

RESULTS

Effect of Grain Boundary Mobility. The initial configuration of the aggregate, in Figure 2, has 384 spherical

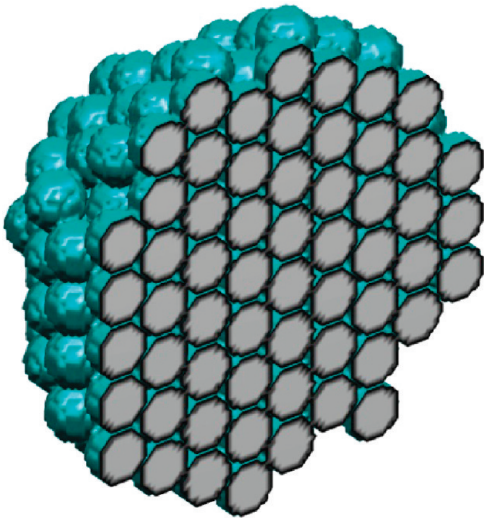

Figure 2. Initial configuration of the aggregate used in our 3D phase field simulations. One half of the spherical polycrystalline mass is cut out to show the internal structure. Dark cyan color indicates surface (material vapor interface) and the gray scale indicates material.

nanoparticles in a hexagonal close-packed arrangement. Clearly, with a sufficiently long duration of sintering, all the pores will be eliminated and the aggregate will become a 100% dense aggregate. Since there are several different ways or mechanisms for

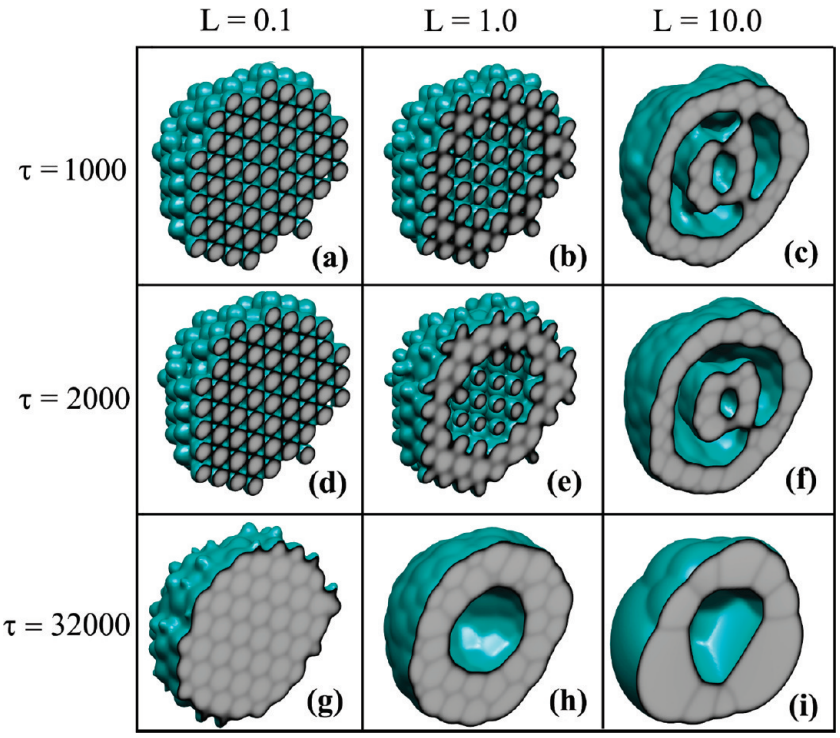

Figure 3. Microstructures obtained from 3D phase field simulations in systems with grain boundary mobilities L = 0.1 (left column), L = 1 (middle column), and L = 10 (right column) for M_S = 1000 and M_{GB} = 100. Top row shows the microstructures at an early stage of evolution (τ = 1000), middle row is for τ = 2000, and the bottom row is for τ = 32000. One half of the aggregate is cut out to show the internal structure.

pore elimination, we may expect different paths toward a fully dense microstructure. Figure 3 displays the various paths for microstructural evolution in systems in which GB mobility (represented by L in our model) is low (L = 0.1), moderate (L = 1), and high (L = 10), in the left, middle, and right column, respectively. The top row shows microstructures at τ = 1000, middle row is for τ = 2000, and the bottom row is for τ = 32000; in all the three systems, M_S = 1000 and M_{GB} = 100.

Figure 3(a,d,g) illustrates the evolution of morphology for a system with a low grain boundary mobility (L = 0.1), due to which grain boundaries formed between the nanoparticles are virtually immobile during the early stages and hence the number of grains almost remains constant right up to $\tau \approx$ 20000 (Figure 4a). With very little GB migration (or, grain growth), the pores in the aggregates remain open and interconnected until $\tau \approx$ 15000; a subsequent increase in the density of the aggregate is seen from Figure 4b. These long-lived open pores get filled by the transport of atoms from the outer surface to the interior *via* surface diffusion along their walls. By τ = 15000, the open pores become closed, and occupy only 5% of the aggregate volume. The closed pores are then filled up through GB diffusion, the second fastest transport mechanism.

In contrast, Figure 3 panels c, f, and i depict a very different pathway to full density, in a system with a high GB mobility (L = 10), due to which GBs between contacting nanoparticles are able to migrate fast causing significant grain coalescence or growth. This results in an intermediate microstructure (Figure 3c,f) which shows a surface shell and a central core; while much of the pore is confined to the region between them, the shell and the core are connected through "bridges". By τ = 1000, the surface shell is fully formed, grain coalescence has eliminated more than a quarter of the original grains (Figure 4a), and pores occupy nearly 30% of the aggregate volume (Figure 4b). In this pathway, the aggregate assumes two types of hollow configurations: one in which it has multiple, interconnected pores (when the central core is still present as in Figure.3f), and another in which it has just one pore in the middle (as in Figure.3i).

In the middle column in Figure 3(b,e,h), the microstructural evolution in a system with a moderate GB mobility (L = 1) shows a third route to full density. During early stages, as atoms are transported from the surface to the interior along the walls of the open pores, surface grains shrink and allow growth of subsurface grains at their expense. Thus, a moderate GB mobility promotes the formation of the surface shell by τ = 2000 (see Figure 3e; see also Figure 4b, where the first data point for relative density starts at τ = 2000). On the other hand, grain growth is virtually arrested inside the aggregate because the grains there are all of similar sizes; thus, the interior particles appear as isolated grains in Figure 3e, unable to form a central core as in Figure 3f. These isolated particles shrink

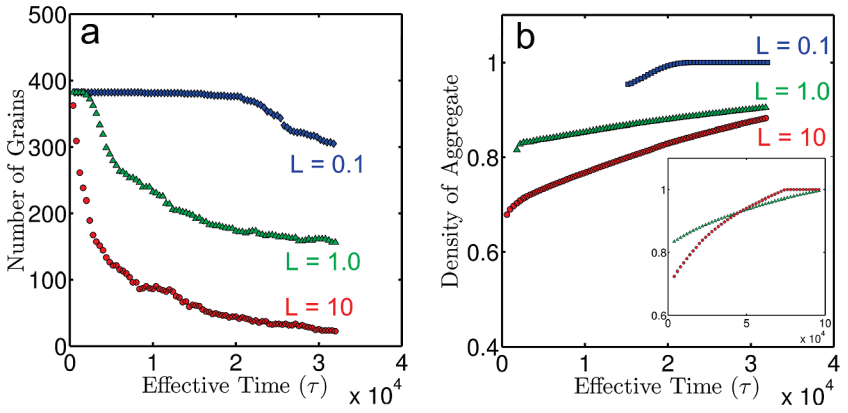

Figure 4. (a) The number of grains inside the aggregate, and (b) density of aggregate after crust formation as a function of effective time $\tau = M_S t$ for three different grain boundary mobilities (L = 0.1, 1.0, and 10) in systems with M_S = 1000 and M_{GB} = 100. The same plot for long time (L = 1.0 and 10) is shown in inset.

rapidly due to Ostwald ripening, and their mass is transported to the interior wall of the surface shell.

These trends are summarized in Figure 4a and 4b; the surface shell formation takes longer in systems with lower GB mobility; further, before the shell is formed, almost all the original grains are still present in the microstructure. Since surface diffusion is the primary mechanism for densification during this stage, the relative density of the aggregate when the shell has just formed is also higher in systems with lower GB mobility. The particle has a relative density of 0.95, 0.82, and 0.67 in systems with L = 0.1, 1, and 10, respectively, at the beginning of the density *versus* τ plot in Figure 4b. A fully formed shell eliminates the (fast) surface diffusion as a mechanism for further densification, leaving a much slower GB diffusion to do this job.

As shown in Figure 3 panels h and i, systems with L = 1 and L = 10 both produce hollow particles at τ = 32000. The main difference between these two hollow structures is in the number of grains in the surface shell: the latter system, with a high GB mobility, has only one set of grains, with GBs running across the shell, while the former (with a moderate GB mobility) has several layers of fine grains in the shell.

This difference in the shell structure leads to an interesting difference in the kinetics of elimination of the central pore. Simulations beyond τ = 32000 show that further densification is actually slower in the system with L = 1 with its smaller grains and larger number of grain boundaries connecting the outer and inner surfaces. In fact, the density vs time plots for systems with L = 10 and L = 1 show a crossover at $\tau \approx$ 50000 in the inset in Figure 4b.

This interesting result may be rationalized using two features: (a) even though the GB paths in this system are greater in number, they are also more tortuous (*i.e.*, the effective diffusion distance is longer in this system), and (b) the effective driving force for GB diffusion is lower. The latter is explained in Figure 5 in terms of the pore shapes in schematic two-

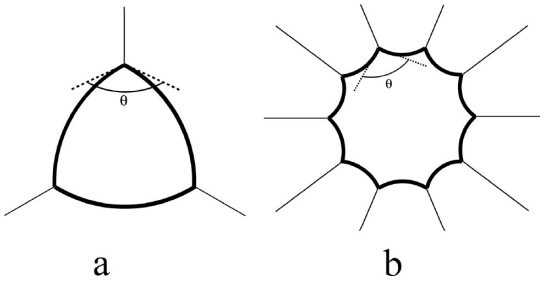

Figure 5. Two-dimensional schematic of (a) a pore surrounded by three grains and (b) a pore surrounded by 10 grains. The dihedral angle, θ is same in both cases. Note that the negative curvature of the pore surface in schematic a changes to positive curvature in schematic b. For this figure, θ is assumed to be 140° for which a nine-sided pore will appear as a polygon.

dimensional systems; since the dihedral angle θ (given by $\theta = \cos^{-1}(\gamma_{GB}/2\gamma_S)$) must be maintained when a GB meets the surface, the grain-pore surface has a negative (positive) curvature when the pore is surrounded by a small (large) number of grains. Therefore, the effective driving force for GB diffusion is smaller when the surface shell has many fine grains (such as in Figure.3h).

Returning now to Figure 3, we already noted that the high GB mobility (L = 10) promotes not only the formation of the surface shell, but also that of a central core (Figure 3f). We can identify two distinct processes in further evolution of the aggregate: (a) Ostwald ripening that makes the central core (with its positive curvature) dissolve, with atoms transported to the inner wall of the shell (which has a negative curvature), and (b) GB diffusion that allows transport of atoms from the outer wall of the shell to the inner wall. Since the former is faster (since surface diffusion is faster than GB diffusion) than the latter, the aggregate acquires a hollow microstructure, in Figure 3i, at τ = 32000.

Effect of Grain Boundary Diffusivity. When GB diffusivity is enhanced, we may expect the latter process (pore filling through GB diffusion) to become faster than the

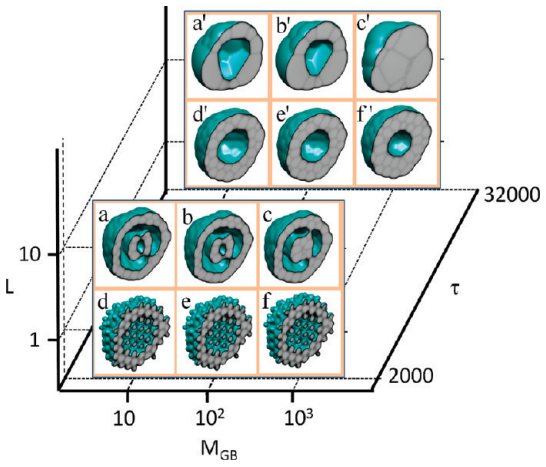

Figure 6. Early stage ($\tau = 2000$) and late stage ($\tau = 32000$) "sintering maps" of microstructures obtained from 3D phase field simulations in systems with varying grain boundary mobilities and grain boundary diffusivities represented by L and M_{GB}, respectively.

TABLE 1. Parameters Used in Simulations

parameters	nondimensional values
bulk free energy coefficients (A,B,Z)	1.0
gradient energy coefficient for density (κ^{ρ})	1.0
gradient energy coefficient for order parameter (κ_i^{η})	0.33
atomic mobility coefficients	
M_B	1.0
M_S	999.0
M_{GB}	0.0, 99.0, 999.0
grain boundary relaxation coefficient (L)	0.1, 1.0, 10
ratio of surface energy to grain boundary energy (γ_S/γ_{GB})	1.5
grid spacing ($\Delta x,\Delta y,\Delta z$)	1.0
time step (Δt)	0.02
system size	128 × 128 × 128

former (dissolution of the central core through Ostwald ripening), and this is indeed found in Figure 6c,c′ in a system with $M_{GB} = M_S = 1000$. However, this system is unrealistic in that the GB diffusivity is the same as surface diffusivity. In the more realistic setting, where M_S is expected to be much higher than M_{GB}, the aggregate is more likely to become hollow first, before full densification; as in Figure 6b,b′. This is consistent with the experimental results presented here and earlier.[12]

We have studied systematically the sintering process in systems with different values of M_{GB} and L. They can be summarized in the form of "sintering maps", as shown in Figure 6 for $\tau = 2000$ and $\tau = 32000$. The early stage evolution shows the formation of a surface shell in all the cases; while a central core is also formed in systems with high GB mobility ($L = 10$), it is absent in systems with moderate GB mobility ($L = 1$). The late stage microstructures in Figure 6 show that, for a given M_{GB}, the surface shell has fewer grains in systems with higher GB mobility, and for a given L, the central pore is smaller in systems with higher GB diffusivity. Indeed in the system with $L = 10$ and $M_{GB} = 1000$ the aggregate is fully dense (Figure 6f′) at $\tau = 32000$.

TABLE 2. Features Observed in the Four Different Microstructural Pathways during Sintering of a Nanoparticle Aggregate

serial no.	microstructural pathway	example
1	multiple closed pores	Figure 3a,d,g
2	surface shell → hollow aggregate	Figure 3b,e,h
3	surface shell and central core → hollow microstructure	Figure 3c,f,i
4	surface shell, central core and multiple interconnected pores	Figure 6c

DISCUSSION

In Table 2 we present a summary of features of the four main microstructural pathways taken by the aggregates during sintering. For example, in a system with a high GB mobility (Figure 3c,f,i), the aggregate first acquires a surface shell and a central core, followed by the dissolution of the central core through Ostwald ripening leaving behind a hollow aggregate. Thus (surface shell + central core) and hollow aggregate are listed as key features of microstructural pathway No.3 in Table 2.

The diversity of pathways to full density during the sintering of aggregates may be understood in terms of two processes: formation of a surface shell and subsequent filling of the hollow void. Our simulations show that the former requires high GB mobility; when this requirement is not met, most of the pores remain open, allowing surface diffusion along the walls of these open pores to promote densification. Indeed, densification is the fastest in the system with the most sluggish GBs ($L = 0.1$). The earlier the shell is formed, the greater is the likelihood of forming a hollow aggregate en route to full densification. When the surface shell is fully formed, densification is controlled by GB diffusion, the second fastest transport mechanism.

A detailed quantitative comparison between our simulations and experimental systems is not possible because of lack of experimental data on surface diffusivity, GB diffusivity, and GB mobility. However qualitative comparison of microstructures is possible. In experimental systems, we expect surface diffusion to be the dominant transport mechanism, with grain boundary diffusion to be several orders of magnitude slower. Thus, if the surface shell is formed easily (*i.e.*, if GB mobility is sufficiently high), we expect the aggregates to assume hollow structures, with either one large pore (in Figure 3i) or multiple, interconnected pores (in Figure 3c); experimentally, both possibilities have been observed in Figure 1 indicating that surface

shell formation is relatively easy in these systems. The difference in the number of grains is indicative of the differences in the grain boundary mobilities in these systems.

Our simulation results also allow us to deduce trends in microstructural evolution with increasing temperature. Because of the difference in the relevant activation energies ($Q_S < Q_{GB}$, and $Q_S < Q_L$) an increase in temperature would increase in both (M_{GB}/M_S) and (L/M_S). This combination of changes implies two possibilities: if the increase in (L/M_S) is more significant, it promotes a hollow aggregate with fewer grains; if, on the other hand, the increase in (M_{GB}/M_S) is more significant, the aggregate is likely to have multiple (and possibly interconnected) pores en route to achieving full density.

Figure 1 panels b–d show the microstructures of sintered CeO_2, Pt, and SnO_2 aggregates; while all these structures are hollow, there is a significant difference in the size and number of grains in the aggregates. Further, the number of grains in CeO_2 aggregates is smaller at higher sintering temperatures (see Figure 1b at 900 °C and Figure 2 of ref 12 at 250, 700, and 900 °C) implying that there is a significant increase in L/M_S in this case. Figure 2c in ref 12 even shows hollow single crystals of CeO_2 using this approach. However, in our simulations, we have never found a single crystalline hollow aggregate primarily because of the pinning of grain boundaries that span the thickness of the surface shell. This pinning effect may be overcome when the surface energy is anisotropic as in sintered CeO_2 aggregates (note the faceted surfaces in Figure 2c in ref 12).

Another implication of our simulation results is that, by controlling GB mobility (L) relative to GB diffusivity (M_{GB}), we can tailor the microstructure for specific applications. For example, fine dispersions that hinder grain boundary motion may promote formation of aggregates with fine open pores (see Figure 3a) suitable for applications such as catalysis and drug delivery.[1,2,5,6] On the other hand, alloying additions/dopants that enhance kinetics of grain growth may promote the formation of hollow aggregates with closed polycrystalline outer shell (see Figure 3h), suitable for applications where we need high shear strength.[8]

Our simulations have used aggregates with about 400 particles; this choice was motivated by the experimental findings in Figure 1; we did not study larger aggregates primarily because of computational limitations. We did, however, study smaller aggregates, and the conclusions remain valid for them as well: for a given combination of M_S and M_{GB}, surface shell is formed earlier and densification is slower in systems with higher L. Similarly, we have verified that there is negligible difference between simulations with and without thermal fluctuations in both density and grain orientation order parameters (incorporated in the simulations using a noise term). Also, simulations of systems with a higher γ_S/γ_{GB} ratio = 3 (obtained using $A = 3$, $B = 1$, $Z = 1$, $\kappa^\rho = 3$, $\kappa^\eta{}_i = 0.33$ in eqs 4 and 5) again showed no significant difference in the sintering behavior of aggregates.

CONCLUSIONS

Our results demonstrate the effect of different kinetic parameters on the evolution of microstructure of nanoporous aggregates. In particular, we show that different combinations of surface and GB diffusivity and GB mobility lead to four different microstructural pathways en route to 100% density: multiple closed pores, hollow shells, hollow shells with a core and multiple interconnected pores are formed as intermediate structures in these cases. The results are qualitatively consistent with the experimental observations on different systems and provide insights for the synthesis of hollow structures and for controlling the stability of nanoporous aggregates.

METHODS

Model Description. We have used a phase-field model that allows grains of a solid phase to be in equilibrium with their vapor phase at a constant temperature. This model is a continuum version of a combination of lattice-gas[13] and Q-state Potts models;[14] the former allows for equilibrium between solid and vapor phases, while the latter allows the solid to exist in the form of multiple grains. In our model, the solid and vapor phases are distinguished using the (scaled) density, ρ as a field variable; in the vapor phase $\rho = 0$ while in the solid phase $\rho = 1$. Within the solid, different grains are distinguished using grain orientation order parameters η_i such that η_i takes the value of unity in the ith grain and zero elsewhere.

The temporal evolution of microstructure is governed by the Cahn–Hilliard equation[15] and the Allen–Cahn equation,[16]

$$\frac{\partial \rho}{\partial t} = \nabla \cdot M \nabla \mu \qquad (1)$$

$$\frac{\partial \eta_i}{\partial t} = -L \frac{\delta (F/N_V)}{\delta \eta_i} \qquad (2)$$

where t is time, M is the atomic mobility (related to atomic diffusivity $D = M\partial^2 f/\partial c^2$ where f is the bulk free energy density defined below), L is a relaxation coefficient for order parameter field η (related to the grain boundary mobility) and μ is the chemical potential, defined as the variational derivative of the total free energy per lattice site, F, with respect to the local material density,

$$\mu = \frac{\delta (F/N_V)}{\delta \rho} \qquad (3)$$

N_V is the number of lattice sites per unit volume. For our model system, F is given by

$$F = N_V \int_\Omega [f(\rho, \eta_i) + \kappa^\rho (\nabla \rho)^2 + \sum_{i=1}^{n} \kappa_i^\eta (\nabla \eta_i)^2] \, d\Omega \qquad (4)$$

where $f(\rho,\eta_i)$ is the bulk free energy per lattice site, κ^{ρ} and κ_i^{η} are gradient energy coefficients for gradients in ρ and η_i, respectively, and n is the number of grain orientation parameters. The bulk free energy density $f(\rho,\eta_i)$ is constructed in such a way that grains of solid and vapor phase are in equilibrium with each other across planar surfaces and grain boundaries. We have used the following form for $f(\rho,\eta_i)$:

$$f(\rho,\eta_i) = A\rho^2(1-\rho)^2 + B\rho^2\xi(\eta_i) + Z(1-\rho)^2\sum_{i=1}^{n}\eta_i^2 \quad (5)$$

where,

$$\xi(\eta_i) = \sum_{i=1}^{n}\left[\frac{\eta_i^4}{4} - \frac{\eta_i^2}{2} + 2\sum_{j>i}^{n}\eta_i^2\eta_j^2\right] + 0.25 \quad (6)$$

and A, B, and Z are constants.

The atomic mobility M in eq 1 is a function of ρ and η_i, and the function is chosen in such a way that allows us to study systems with enhanced atomic diffusivity at the surface and grain boundaries:

$$M(\rho,\eta_i) = M_B + 16M_S\rho^2(1-\rho)^2 + 4M_{GB}\sum_{j>i}^{n}[\eta_i^2\eta_j^2]^{1/2} \quad (7)$$

where M_B, M_S, and M_{GB} are the atomic mobility parameters for the bulk surface and grain boundaries, respectively, and may be related to bulk, surface, and grain boundary diffusivities, respectively.

The parameters used in our model are in their scaled or nondimensional form and are listed in Table 1. We have followed the procedure described earlier[17] to render all our variables nondimensional. We have used a semi-implicit Fourier spectral method[18] for solving kinetic equations (eq 1 and eq 2) with variable atomic mobility, and the FFTW software package[19] for performing the discrete Fourier transforms.

In our simulations, we track the evolution of nanoparticle aggregates by solving the Cahn−Hilliard and Allen−Cahn equations (eqs 1 and 2, respectively). The bulk diffusivity is constant (M_B = 1), and we have studied the evolution of the nanoparticle aggregate as a function of grain boundary and surface diffusivities (represented by the atomic mobility parameters M_{GB} and M_S, respectively), and the grain boundary mobility (represented by L, the relaxation coefficient in eq 2). Since the simulations explore systems with different values of M_S, M_{GB}, and L, a direct comparison of different microstructures is meaningful only when they are obtained at the same "effective time" which we define as $\tau = M_S \times t$; this definition uses M_S since surface diffusion is the fastest transport mechanism. Microstructures are characterized using both the number of grains that remain at any intermediate time τ, and the aggregate density. The latter can be measured only when the aggregate develops a fully formed surface shell that leaves only closed pores; thus, after the shell formation, the density is measured using

$$D_p = 1 - (V_v/V_m)$$

where D_p is the relative density of the aggregate, V_v is the volume of the interior vapor phase and V_m is the volume occupied by material. In our simulation, the rigid surface shell is identified through an examination of the vapor phase (defined as regions with $\rho < 0.5$) using the Hoshen−Kopelman cluster counting algorithm.[20]

Acknowledgment. N.R. thanks DST, Government of India, for funding. E.A.A. acknowledges UGC for a senior research fellowship.

REFERENCES AND NOTES

1. David, E. B. Self-Assembled, Sub-micrometer Diameter Semipermeable Capsules. *Angew Chem., Int. Ed.* **1999,** *38*, 2870–2872.
2. Mathiowitz, E.; Jacob, J. S.; Jong, Y. S.; Carino, G. P.; Chickering, D. E.; Chaturvedi, P.; Santos, C. A.; Vijayaraghavan, K.; Montgomery, S.; Bassett, M.; *et al.*Biologically Erodable Microspheres as Potential Oral Drug Delivery Systems. *Nature* **1997,** *386*, 410–414.
3. Ni, D.; Wang, L.; Sun, Y.; Guan, Z.; Yang, S.; Zhou, K. Amphiphilic Hollow Carbonaceous Microspheres with Permeable Shells. *Angew Chem. Int. Ed.* **2010,** *49*, 4223–4227.
4. Yang, Z.; Han, D.; Ma, D.; Liang, H.; Liu, L.; Yang, Y. Fabrication of Monodisperse CeO_2 Hollow Spheres Assembled by Nano-octahedra. *Cryst. Growth Des.* **2009,** *10*, 291–295.
5. Warren, S. C.; Messina, L. C.; Slaughter, L. S.; Kamperman, M.; Zhou, Q.; Gruner, S. M.; DiSalvo, F. J.; Wiesner, U. Ordered Mesoporous Materials from Metal Nanoparticle-Block Copolymer Self-Assembly. *Science* **2008,** *320*, 1748–1752.
6. Attard, G. S.; Bartlett, P. N.; Coleman, N. R. B.; Elliott, J. M.; Owen, J. R.; Wang, J. H. Mesoporous Platinum Films from Lyotropic Liquid Crystalline Phases. *Science* **1997,** *278*, 838–840.
7. Viswanath, B.; Patra, S.; Munichandraiah, N.; Ravishankar, N. Nanoporous Pt with High Surface Area by Reaction-Limited Aggregation of Nanoparticles. *Langmuir* **2009,** *25*, 3115–3121.
8. Shan, Z. W.; Adesso, G.; Cabot, A.; Sherburne, M. P.; Syed Asif, S. A.; Warren, O. L.; Chrzan, D. C.; Minor, A. M.; Alivisatos, A. P. Ultrahigh Stress and Strain in Hierarchically Structured Hollow Nanoparticles. *Nat. Mater.* **2008,** *7*, 947–952.
9. Kielbassa, S.; Häbich, A.; Schnaidt, J.; Bansmann, J.; Weigl, F.; Boyen, H.-G.; Ziemann, P.; Behm, R. J. On the Morphology and Stability of Au Nanoparticles on TiO_2(110) Prepared from Micelle-Stabilized Precursors. *Langmuir* **2006,** *22*, 7873–7880.
10. Santra, A. K.; Goodman, D. Oxide-Supported Metal Clusters: Models for Heterogeneous Catalysts. *J. Phys. Condens. Mater.* **2002,** *14*, R31–R62.
11. Yang, F.; Chen, M. S.; Goodman, D. W. Sintering of Au Particles Supported on TiO_2(110) during CO Oxidation. *J. Phy. Chem.C* **2008,** *113*, 254–260.
12. Anumol, E. A.; Viswanath, B.; Ganesan, P. G.; Shi, Y.; Ramanath, G.; Ravishankar, N. Surface Diffusion Driven Nanoshell Formation by Controlled Sintering of Mesoporous Nanoparticle Aggregates. *Nanoscale* **2010,** *2*, 1423–1425.
13. Binder, K. Monte Carlo Calculation of the Surface Tension for Two- and Three-Dimensional Lattice-Gas Models. *Phys. Rev. A.* **1982,** *25*, 1699–1709.
14. Sahni, P. S.; Grest, G. S.; Anderson, M. P.; Srolovitz, D. J. Kinetics of the Q-State Potts Model in Two Dimensions. *Phy. Rev. Lett.* **1983,** *50*, 263.
15. Cahn, J. W. On Spinodal Decomposition. *Acta Metall.* **1961,** *9*, 795–801.
16. Allen, S. M.; Cahn, J. W. A Microscopic Theory for Antiphase Boundary Motion and Its Application to Antiphase Domain Coarsening. *Acta Metall.* **1979,** *27*, 1085–1095.
17. Gururajan, M. P.; Abinandanan, T. A. Phase Field Study of Precipitate Rafting under a Uniaxial Stress. *Acta Mater.* **2007,** *55*, 5015–5026.
18. Zhu, J.; Chen, L. Q.; Shen, J.; Tikare, V. Coarsening Kinetics from a Variable-Mobility Cahn−Hilliard Equation: Application of a Semi-implicit Fourier Spectral Method. *Phys. Rev. E.* **1999,** *60*, 3564–3572.
19. Frigo, M.; Johnson, S. G. *Proc. IEEE Int. Conf. Acoustics, Speech, Signal Process.* **1998,** *3*, 1381–1384.
20. Hoshen, J.; Kopelman, R. Percolation and Cluster Distribution. I. Cluster Multiple Labeling Technique and Critical Concentration Algorithm. *Phy. Rev. B* **1976,** *14*, 3438.